Structural and Electronic Properties of Lithiated SnO$_2$. A Periodic DFT Study

Fabrício R. Sensato,*[†] Lourdes Gracia,*[‡] Armando Beltrán,[‡] Juan Andrés,[‡] and Elson Longo[§]

[†]Instituto de Ciências Ambientais, Químicas e Farmacêuticas, Universidade Federal de São Paulo, UNIFESP, R. Arthur Riedel 275, 09972-270 Diadema, Brazil

[‡]Departament de Química Física i Analítica, Universitat Jaume I, Campus del Riu SEC, E-12071 Castelló, Spain

[§]Instituto de Química, Universidade Estadual Paulista, UNESP, 14800-900 Araraquara, Brazil

Ⓢ *Supporting Information*

ABSTRACT: The structural and electronic properties of the intercalation compound Li$_x$SnO$_2$ (x = 1/16, 1/8, 1/4, 1/2, 1) as well as the inherent diffusion mechanism of Li ion into the rutile SnO$_2$ were investigated by means of periodic density functional calculations. Optimized structural parameters, cohesive energies, electronic band structure, and density-of-states and Mulliken charges for the Li$_x$SnO$_2$ system at different Li ordering for each Li content are reported. The energetic profiles for the Li diffusion process into rutile SnO$_2$ are also presented. Our calculation indicates substantial host distortion around intercalation sites, predominantly along the *ab*-planes.

These deformations are found to be related to the soft B$_{1g}$, E$_u$, A$_{2g}$, and A$_{1g}$ vibrational modes of very low frequency and therefore easy to be achieved. The corresponding variation in volume monotonically increases with the Li concentration. Cohesive energies are consistent with continuous and reversible intercalation process. In lithiated SnO$_2$, lithium is significantly ionized; however, the distribution pattern of the charge transferred from the lithium to the host is very dependent upon the ion concentration. By increasing the Li content, the relative amount of charge transferred to the Sn atoms decreases whereas the charge transferred to oxygen atoms increases. Lithium intercalation causes a chemical reduction of SnO$_2$ and yields metallic properties. Effects induced by Li intercalation on the electronic band structures of SnO$_2$ were assessed according to their origins, i.e., if they originate from lattice expansion or from chemical reduction. The energy difference between the valence-band maximum and conduction-band minimum of lithiated SnO$_2$ decreases with increasing Li content. Lithium diffusion along the *c*-direction demands significantly lower activation energy than the energy required for diffusion along *ab*-planes. Energetic barriers related to the lithium diffusion into SnO$_2$ were found to be dependent upon the Li content.
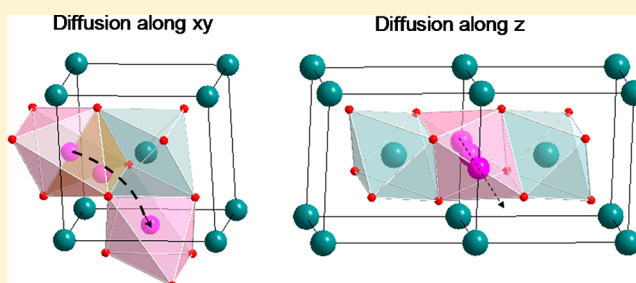
1. INTRODUCTION

As highlighted in a recent editorial in a sister journal to *The Journal of Physical Chemistry C*, the demand for improved storage batteries in energy-efficient devices has energized the scientific community to design lightweight high-capacity storage batteries.[1] Lithium-ion batteries are the power sources of choice for modern consumer electronic devices which now represent the largest segment of the portable battery industry and dominate the computer, cell phone, and camera power source industry.[2] However these batteries are still the subject of intense research activity focused on the development of new high-performance electrode materials while meeting the requirements of safety and environment.

SnO$_2$ is a prototype transparent conductor which exhibits contradictory properties of high metallic conductivity with nearly complete insulator-like transparency in the visible range. Since the announcement by Fuji Photo Film Celltee Co Ltd. Japan[3] of the STALION lithium ion cell and the pivotal study by Idota et al.[4] on the capability of Sn-based materials to be used as an active electrode in Li-ion rechargeable batteries, the

lithiated SnO$_2$ system has garnered extensive attention from the scientific community.[5−24] In particular, the principal advantage of tin oxide-based electrodes over conventional electrodes is their elevated theoretical specific capacity and higher density. For instance, anodes derived from tin oxide were found to store over twice as much Li$^+$ as graphite while ensuring protection against dendritic (metallic) Li formation.[4] It has also been recognized that exploring effective ways to intercalate lithium reversibly into nanostructured electrode materials will be an important key to the success of developing high-density storage devices.[1] Interestingly, SnO$_2$ can now be synthesized as nanowires, nanorods, nanotubes, and nanobelts. Indeed, enhanced cycling stability induced by a nanoscale effect has also been reported.[9,10,12,21−23] The reversible Li storage capacity of SnO$_2$ nanowires was also found to be much higher than that of TiO$_2$ nanowires.[14] In addition, SnO$_2$ has been cited

to exhibit outstanding features from an architectural perspective; e.g., crystalline SnO_2 assembled into a higher-order nanostructure (mesostructure), whose integrated geometry is expected to lead to functional improvements, is supposed to store an exceedingly large amount of Li^+.[17]

In addition to its application in lithium batteries, the crystalline Li ion−SnO_2 system has been reported to be a very efficient counterelectrode in electrochromic devices.[18,25−31] A major application of these devices is smart windows that can regulate the solar gains of buildings and also in glare attenuation in automobile rear-view mirrors.

For both applications (i.e., Li-ion rechargeable batteries and electrochromic devices) the device performance depends on the ability of the electrode to intercalate lithium reversibly into the host lattice. These technically interesting properties are connected to Li ion intercalation/deintercalation and the accompanying electron insertion/extraction. The potentiality of SnO_2 in this kind of device is ascribed to its open structure which is capable of accommodating lithium ions and the variable valence of Sn atoms which endows the material with ability to accommodate donated electrons. Thus, lithium ions are injected into SnO_2 electrode during the negative sweep and ejected from it in the positive direction sweep; i.e., the forward biasing of SnO_2 electrodes in lithium-ion-containing electrolytes leads to electron accumulation in the SnO_2 lattice, whose charge is compensated by Li^+ diffusion from the electrolyte.

Two main mechanisms of lithium intercalation can be active in this system. The first mechanism is the conventional intercalation/deintercalation reaction where the ion is only simply inserted into the transition metal dioxide material such as MoO_2, WO_2, and TiO_2.[32]

$$SnO_2 + xLi^+ + xe^- \leftrightarrow Li_xSnO_2 \quad \text{(reversible)} \quad (1)$$
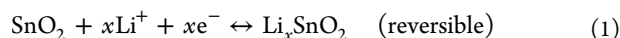
where x is the mole fraction of Li in the SnO_2. For this system, the charge (Li-released) and discharge (Li-inserted) reactions are accompanied by a intervalency transition between Sn^{4+} and Sn^{2+} in line with the valence state changing observed in other oxides during the ion intercalation/deintercalation process.[18,26,31] On the other hand, a two-step mechanism for the electrochemical lithiation of SnO_2 has been identified.[19,20,33] In the first step, an irreversible conversion of the tin oxide to metallic tin occurs which is dispersed in a matrix of lithium oxide

$$4Li^+ + 4e^- + SnO_2 \Rightarrow 2Li_2O + Sn \quad \text{(irreversible)} \quad (2)$$
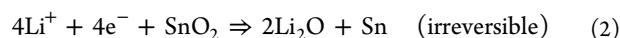
and is then followed by the reversible alloying/dealloying of the Sn with Li to form a variety of alloys[34−36] to reach a composition of $Li_{4.4}Sn$ at the highest lithium concentration:

$$xLi^+ + xe^- + Sn \Rightarrow Li_xSn, \ 0 \leq x \leq 4.4 \quad \text{(reversible)} \quad (3)$$
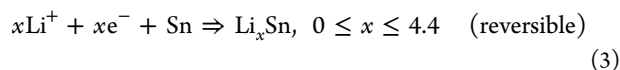
The corresponding electrode charge storage capacity would be related to the latter process. Yet, there is some evidence that eq 2 could be partially reversible when SnO_2 nanoparticles are used[22] or when they are embedded in a carbonaceous shell.[16] In this context, further studies are required for a better understanding of lithium insertion into rutile SnO_2.

To date, quantum mechanical methods are recognized as suitable tools to design new electrode materials since they have been used to predict the influence of ion intercalation on electronic and structural properties, especially in a system that may be difficult to investigate by experimental techniques.[37] Here we present a periodic DFT study on the lithiated SnO_2.

The objective of this study is twofold: (i) to investigate the influence of Li ion intercalation on the electronic and structural properties of SnO_2 bulk and (ii) to shed some light on the inherent diffusion mechanism. We anticipate that our present Li ion diffusion study is closely related to eq 1 because such a chemical equation is a very reliable description for the ionic diffusion in the initial stages of Li intercalation[38] and also is very representative of Li-doped SnO_2 systems (i.e., lithiated SnO_2) where Li ions are synthetically incorporated into the SnO_2 matrix (Li_xSnO_2 solid solution). However, we are aware that eq 1 might not suitably describe real electrochemical phenomena since the *modus operandi* of an operating battery is found not to be properly described by an ideal succession of well-defined stages.[38]

As part of our ongoing computational research on the electronic and structural properties of SnO_2 in its pure[39−41] or doped[42−44] forms, in this study, we report fully relaxed structural parameters, cohesive energy, electronic band structure, total and projected density of states for Li_xSnO_2 ($0 \leq x \leq 1$), and the main diffusion pathways and corresponding energy barriers.

2. THEORETICAL CALCULATIONS AND MODELS

2.1. Computational Details. The structural properties of Li_xSnO_2 system as well as the inherent Li diffusion process were investigated by means of periodic first-principles calculations in the framework of density functional theory within the generalized gradient approximation (GGA) as parametrized by Perdew and Wang[45] using the VASP program.[46,47] Electron−ion interactions were described by the projector augmented wave (PAW) pseudopotentials[48] and the plane-wave expansion was truncated at a cutoff energy of 400 eV. Our DFT calculations are for bulk phases. A spin-unrestricted approach has been employed when Li was inserted and migrated into the lattice. The cohesive energy or energy associated with the intercalation processes, E_{coh}, was calculated as the difference between the total energy of the crystal at equilibrium and the total energies of the isolated atomic components. However, the inverse (negative) definition is used below so that cohesive energies appear positive. The jump diffusion coefficients, D, were estimated using the expression $D = \Gamma l^2$, where Γ is the rate to hop between sites and l is the distance between sites. We have approximated the rate Γ when lithium atoms hop to vacant neighboring sites by the transition state theory according to $\Gamma = \nu^* \exp(-\Delta E_B/kT)$, where ν^* is an effective vibrational frequency and ΔE_B is the activation barrier defined as the difference in energy at the activated state and the energy at the initial equilibrium state of the hop. Since it is known that DFT calculations using pure functionals might not correctly describe localized states in wide-band-gap semiconductors, the B3LYP hybrid functional,[49,50] as implemented in CRYSTAL 09,[51,52] was used to perform electronic structure calculations in order to yield the Li_xSnO_2 electronic band structure, total density of states (DOS), and projected densities of states (PDOS). Indeed, the DFT/B3LYP approach has been shown to reproduce observed geometrical parameters and band gaps reliably in a wide variety of materials.[53] For CRYSTAL calculations, the Sn, O, and Li basis sets are 9763-111d631G,[54] 6-31d1,[55] and 5-11d1[56] contractions, respectively.

It should be noted that a similar approach has been used in other recent research involving Li mobility on layered transition metal oxides,[57] olivine $LiFePO_4$,[58,59] spinel $Li_xMn_2O_4$,[60] lithium

halides,[61] TiO_2,[62,63] $Li_{1+x}Ti_2O_4$,[64] and WO_3[65] as well as in diffusion studies of metal subsurface impurities.[66,67]

2.2. Model System for Lithium Intercalation. It should be mentioned that our models are intended to describe the intercalation process as well as the diffusion process taking place into the crystalline form of SnO_2 material as long as this oxide with higher crystallinity is found to display better electrochemical performance.[15,21] In addition, our models are also electrically neutral and might represent either a system composed of two neutral entities (the tin oxide and the lithium atom) or the lithium cation and the (negatively) ionized oxide with an extra electron injected from the electrode in accordance with eq 1.

Tin oxide (SnO_2) is a semiconductor crystallizing in the rutile structure with space group $P4_2/mnm$. The corresponding tetragonal unit cell is characterized by two lattice parameters a and c and the internal parameter u. The SnO_2 experimental lattice parameters are $a = 4.737$, $c = 3.186$, and $u = 0.306$.[68,69] Its unit cell contains two tin and four oxygen atoms ($Z = 2$) and, therefore, two molecular units per tetragonal cell with the tin atoms (blue spheres) in bct positions (0,0,0) and the oxygen atoms (red spheres) in the $\pm(u,u,0)$ position. Indeed, the rutile structure is composed of SnO_6 polyhedra sharing edges in the c-direction and corners in the ab-planes (see blue polyhedra in Figure 1). The four equatorial Sn−O distances are 2.056 Å, and the two apical distances are 2.050 Å.
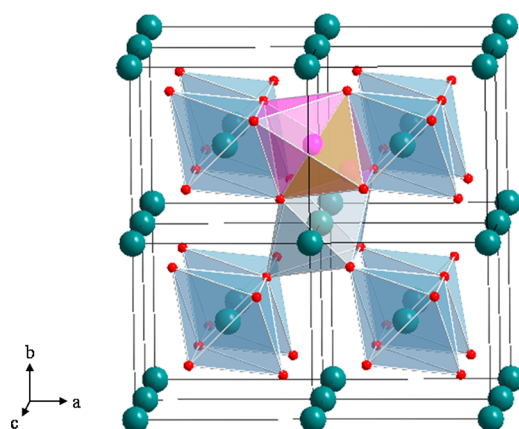

Figure 1. Polyhedral representation of a portion ($2 \times 2 \times 2$) of rutile SnO_2. Blue polyhedra describe the SnO_6 units. The octahedral site for lithium intercalation is marked in pink (LiO_6), whereas the tetrahedral site is marked in brown. Tin, oxygen, and lithium atoms are described by blue, red, and pink spheres, respectively.

There are potentially two kinds of sites available to accommodate Li ions. The octahedral sites (see pink polyhedron in Figure 1) are formed by the SnO_6 polyhedra sharing corners, whereas the tetrahedral sites (brown polyhedron) are built from edge-sharing in the c-direction. This polyhedron LiO_6 is distorted and exhibits a height of 3.435 Å and a rectangular base of 3.435×3.186 Å. Tetrahedral sites are irregular pyramid with sides of 3.186 and 2.905 Å.

All models were built from a tetragonal supercell $2 \times 2 \times 2$, $Sn_{16}O_{32}$, containing 16 SnO_2 units in 8 tetragonal unit cells of SnO_2. To assess the Li−Li interaction effects on the structural and electronic properties of lithiated tin oxide, several Li_xSnO_2 models were built which differ from each other in Li concentration (i.e., namely, $x = 0$, 1/16, 1/8, 1/4, 1/2, 1, which correspond to 0, 1, 2, 4, 8, and 16 Li atoms in the

supercells, respectively). Moreover, for a given composition, distinct ordering patterns for Li distribution were also considered and are presented in Figure 2 along with the corresponding labels. For the sake of clarity and comprehension, fractional coordinates (referred to the $2 \times 2 \times 2$ generic model) of lithium ions through each periodic model are given in Table S1 (Supporting Information). Two periodic models were built for $x = 1/16$; in 1/16A, the lithium ion is inserted into an octahedral site whereas in 1/16A′ is incorporated into a tetrahedral site. As long as the octahedral site was found to exhibit lower energy (see Results and Discussion section) in the models containing higher ion concentration lithium atoms were then inserted into the octahedral sites to satisfy the condition $x = 1/8$, 1/4, 1/2, 3/4, and 1.

Eight periodic models have been built for both $x = 1/4$ and $x = 1/8$, three distinct ordering schemes for $x = 1/2$, and one Li distribution for $x = 1$ (for a straightforward description, see Figure 2 and Table S1). Although a comprehensive number of model systems has been built for each Li ion content, we are aware that such models do not exhaust all possibilities for Li intercalation.

2.3. Model System for Lithium Diffusion. The models for the diffusion process were built to permit only one Li to diffuse into the $2 \times 2 \times 2$ supercell; the more stable Li ordering pattern for each composition was considered. Two diffusion pathways connecting octahedral intercalation sites were investigated: (i) diffusion in the ab-planes (along the [110] direction) and (ii) diffusion parallel to the c-axis (along the [001] direction). Diffusion profiles of the Li ion were obtained by fixing the coordinates of the diffusing atom only along the diffusion direction and allowing the other two coordinates as well as the rest of the atoms in the supercell to relax. The volume of the cell was also allowed to relax. The diffusion pathway along the [110] direction is illustrated in Figure 3a while the pathway along the [001] direction is depicted in Figure 3b.

3. RESULTS AND DISCUSSION

3.1. Nonlithiated SnO_2. First, the computational procedure was tested for $Sn_{16}O_{32}$ supercell optimization. Calculated lattice constants are $a = 4.734$ Å and $c = 3.220$ Å. These calculated structural parameters are very close to the experimental parameters (about 0.9% expansion) and to our previous computational studies.[40,41,43] Regarding the SnO_6 polyhedra, the relaxed apical Sn−O distances are 2.055 Å while the equatorial distances are 2.064 Å. Octahedral sites for Li intercalation were calculated to have a height of 3.433 Å and a rectangular base of 3.433×3.220 Å.

3.2. Structural Properties of Lithiated SnO_2. Li ion intercalation into a tetrahedral site did not correspond to an equilibrium structure. Indeed, the ion was found to move into an adjacent octahedral site along the optimization procedure, although several attempts to optimize 1/16A′ were conducted. Therefore, in the remaining models, only octahedral sites were considered for lithium intercalation.

Calculated cohesive energies for different Li concentrations are collected in Table 1. The calculated cohesive energy for pure SnO_2 (not shown in Table 1) is 283.2 eV. From Table 1, it is observed that all intercalated structures are found to be stable with respect to isolated atomic components. The most stable lithium ordering at each Li concentration is as follows: 1/16A, 1/8B, 1/4F, 1/2B, and 1A. The dependence of the cohesive energy (for the most stable configuration) upon lithium
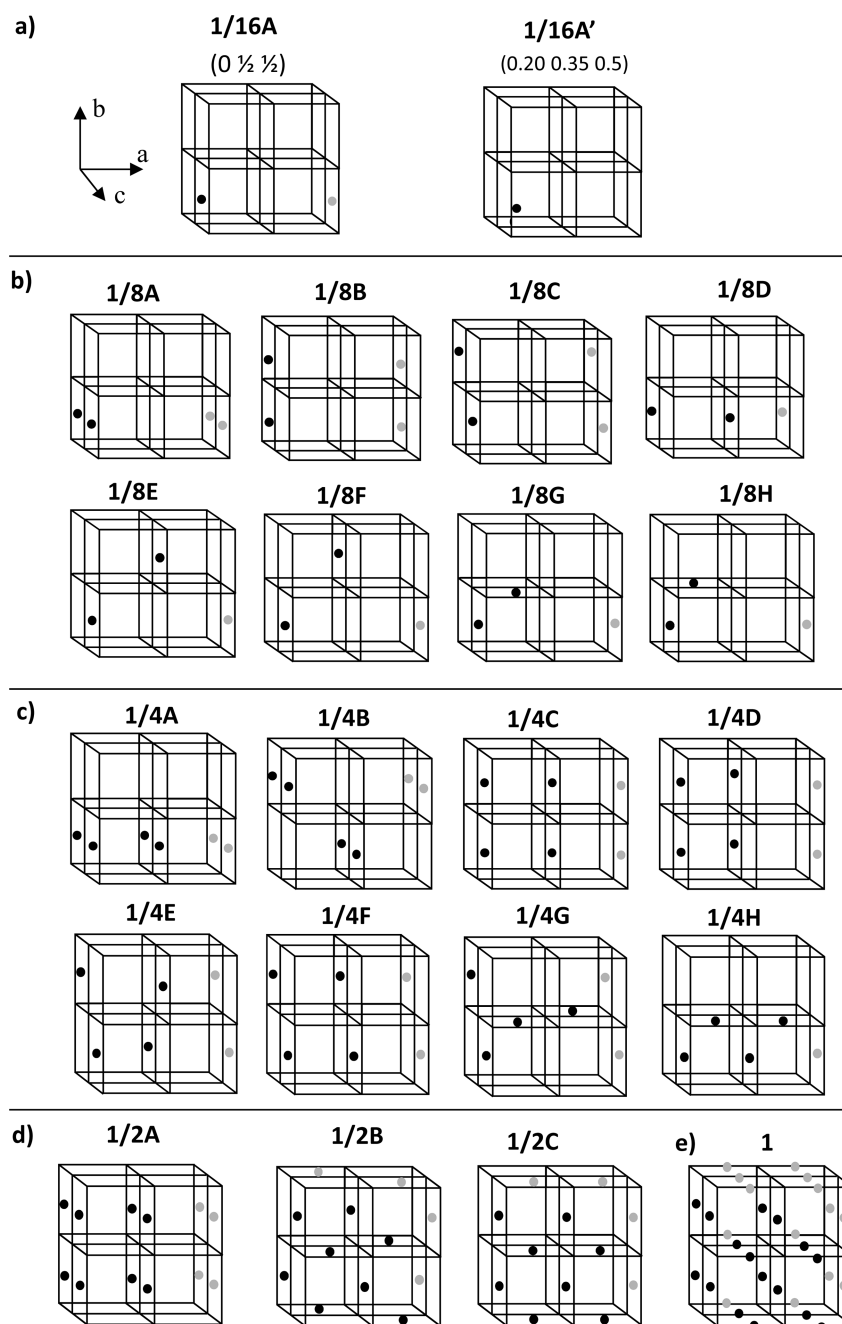
Figure 2. Periodic $2 \times 2 \times 2$ Li_xSnO_2 models and the Li ion ordering pattern at x = (a) 1/16, (b) 1/8, (c)1/4, (d) 1/2, and (e) 1. In 1/16 A′, the Li atom is incorporated in a tetrahedral site.

concentration is shown in Figure 4. The cohesive energies are found to increase monotonously with the Li concentration which is consistent with continuous ion intercalation. The variation of the cohesive energy per number of Li ions in the supercell $2 \times 2 \times 2$ is depicted in Figure S1.

For the most stable configurations, the cohesive energy per lithium atom does not vary significantly with Li concentration. For example, $\Delta E_{coh}(x = 0 \rightarrow x = 1)$ is 42 eV. This value is comparable to $16 \times \Delta E_{coh}(x = 0 \rightarrow x = 1/16) = 51$ eV; $8 \times \Delta E_{coh}(x = 0 \rightarrow x = 1/8) = 45$ eV; $4 \times \Delta E_{coh}(x = 0 \rightarrow x = 1/4) = 44$ eV; and $2 \times \Delta E_{coh}(x = 0 \rightarrow x = 1/2) = 44$ eV. The significantly lower cohesive energy at $x = 1/16$ would be related to the absence of very short Li–Li distances.

The variation in a-lattice (Δa), b-lattice (Δb), and c-lattice (Δc) parameters induced by lithium intercalation is illustrated in Figure 5. However, we emphasize that the corresponding variation values refer to $2 \times 2 \times 2$ supercells and not to a conventional unit cell.

It is clear from Figure 5 that our calculations (full optimization) indicate relevant distortions of the local environment around the inserted atoms (mainly in ab-planes). For most Li_xSnO_2 systems considered in this study, enlargement along the b-lattice constant is more pronounced than in the a-lattice constant. The dominant distortion along the ab-planes can be rationalized in terms of the vibrational modes of SnO_2 because atomic movements in the c-direction and in ab-planes are known to be relatively independent in rutile.[70−73] The
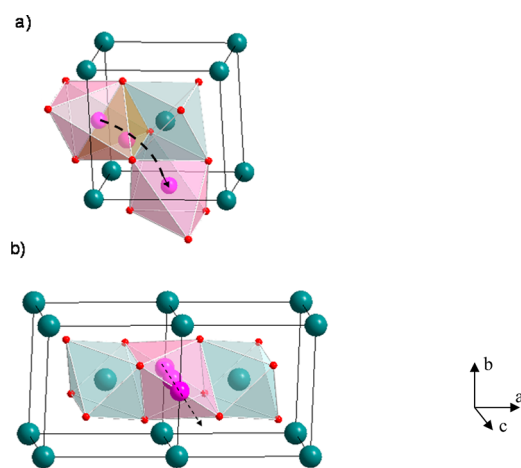
Figure 3. Investigated pathways connecting two octahedral sites (a) in *ab*-planes (perpendicular to the crystal *c*-axis and therefore along the [110] direction) and (b) parallel to the *c*-axis ([001] direction). Additional details are presented in the caption of Figure 1.

Figure 4. Calculated cohesive energies upon Li concentration for the most stable Li ordering at each composition.

corresponding irreducible representation of optic modes is $\Gamma = A_{1g} + A_{2g} + B_{1g} + B_{2g} + E_g + A_{2u} + 2B_{1u} + 3E_u$. These eigenmodes are usually classified into modes with atomic motion only along the *z*-direction (E_g, B_{1u}, and A_{2u}) and modes with atomic motion perpendicular to it (all others). Deformations in *ab*-planes upon Li insertion are found to be related to the soft B_{1g}, E_u, A_{2g}, and A_{1g} vibrational modes of very low frequency and therefore easy to be achieved. Indeed, our calculated vibrational frequencies for theses modes in pure SnO_2 are 123 cm^{-1} (B_{1g}), 266 cm^{-1} (E_u), 401 cm^{-1} (A_{2g}), and 676 cm^{-1} (A_{1g}), which are in accordance with available experimental data.[71−73]

The volume variation, ΔV, induced by Li intercalation for the most stable Li ordering is depicted in Figure 6. It can be observed that variation in volume increases in an approximately linear way with Li concentration. The change in volume related to pure SnO_2 is significant. For the most stable Li ordering schemes the change in volume is as follows: 4.6% at $x = 1/16$; 6.3% at $x = 1/8$; 9.9% at $x = 1/4$; 16.8% at $x = 1/2$; and 39.1% at $x = 1$. The variation in volume per lithium atom is depicted in Figure S2.

To gain a deeper insight into the local structural distortions induced by lithium intercalation, for most stable system at each composition, Table 2 shows the variation in volume of the occupied oxygen polyhedron as well as variation in the volume of the nearest (occupied or vacant) neighbors oxygen polyhedra along the [100], [010], [001], and [110] directions. They correspond to *a*-, *b*-, *c*-, and *ab*-glide-related oxygen polyhedron, respectively (Li-occupied oxygen polyhedron is marked in pink in Figure 1).

Except for $x = 1$, lithium intercalation is found to shrink the oxygen polyhedra around them (see negative values of $\Delta V\%$ in
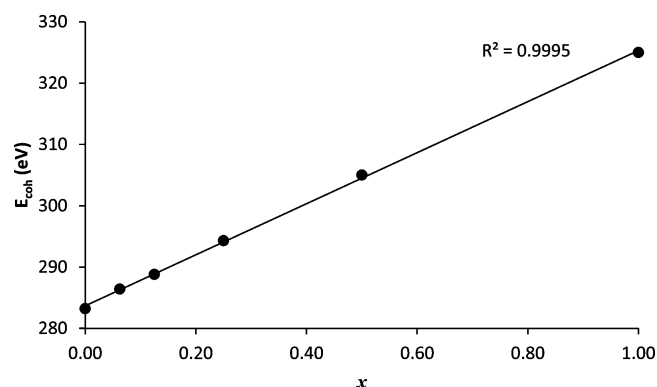
Table 2). On the other hand, for $x = 1$, lithium intercalation is found to expand oxygen polyhedra by about 17%. As a general rule, the vacant oxygen polyhedra surrounding the intercalation site are also found to expand. The major expansion occurs at the [110]-glide oxygen polyhedron and is connected with the enlargement of the distance between equatorial oxygen atoms in the [110] direction. The vacant [001]-glide oxygen polyhedra suffer the smallest expansion.

At $x = 1/16$ the Li ions are separated by 11, 11, and 3 atomic planes in the [100], [010], and [001] directions, respectively. Accordingly, the Li−Li distances are calculated to be 9.66, 9.65, and 6.94 Å, respectively, along the same directions. The Li atom is essentially octahedrally coordinated and is itself placed about 2.23 (±0.02) Å and 1.84 (±0.01) Å from equatorial and apical oxygen atoms, respectively. In comparison to the intercalation polyhedra in pure SnO_2, equatorial oxygen atoms are found to move toward the Li atom while the apical atoms move outward from it. These movements decrease the volume of oxygen polyhedra around the Li ion by ∼3.0%. As a result, such a deformation decreases the space for the diffusion into the next-neighbor site along the [110] direction by about 0.2 Å. The six nearest tin atoms also move outward from the lithium atom. As a consequence, the Sn−Sn interatomic distances at the Li-occupied site increase 0.36 Å along the [100] direction while increasing by only 0.09 and 0.03 Å along the [010] and [001] directions, respectively, with respect to their crystallographic position in pure SnO_2; the Sn−Sn interatomic distances along [100], [010], and [001] directions correspond to *a*, *b*, and *c* parameters of a primitive cell of rutile structure. This distortion pattern reveals that structural changes induced by the intercalation of lithium atom are rather anisotropic.

For $x = 1/8$, the predicted order of stability in terms of cohesive energies is as follows (from less to more stable ordering): 1/8F < 1/8E < 1/8D < 1/8/G < 1/8C < 1/8/H < 1/8A < 1/8B. The most stable ion ordering (1/8B) corresponds to the ordering where Li ions occupy neighboring octahedra in the [010] direction while they are separated in

Table 1. Calculated Cohesive Energies (in eV) for All Investigated Li$_x$SnO$_2$ Systems

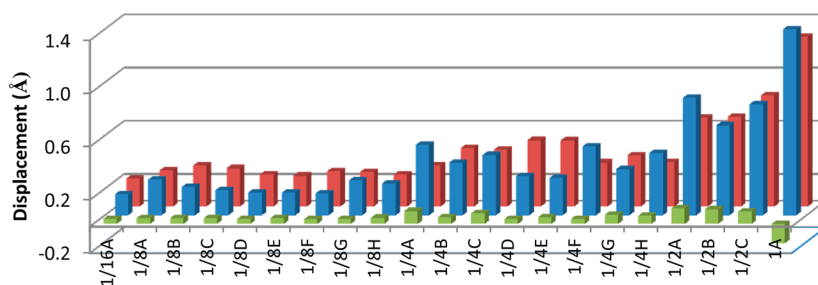|	A	B	C	D	E	F	G	H
1/16	286.4							
1/8	288.7	288.8	288.5	288.1	287.7	287.6	288.4	288.6
1/4	293.6	292.9	292.8	293.8	294.0	294.3	294.0	293.4
1/2	303.4	305.0	301.2					
1	325.1							

Figure 5. Structural distortions in cell parameters of 2 × 2 × 2 periodic models as a function of lithium intercalation: Δa-lattice (blue); Δb-lattice (red); Δc-lattice (green).
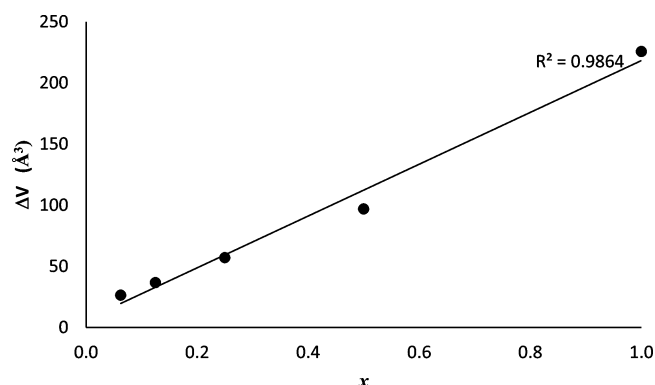

Figure 6. Variation in volume with Li concentration for the most stable Li ordering. The corresponding variations refer to a 2 × 2 × 2 pure SnO_2 supercell.

Table 2. Volume Variation ($\Delta V\%$) of Intercalation Sites as Well as Their Neighboring (Vacant or Occupied) Polyhedra

model	polyhedron[a]	[110]	[010]	[100]	[001]
1/16A	−2.9	6.5	5.7	4.1	3.2
1/8B	−2.3	8.3	−2.3[b]	6.4	6.3
1/4F	−2.6	14.6	11.9	−2.6[b]	11.9
1/2B	−1.5	−2.06[b]	15.0	15.0	15.0
1A	17.3	27.4[b]	17.3[b]	17.3[b]	17.3[b]

[a]Occupied oxygen polyhedra related to neighbors-glide oxygen polyhedra. [b]Occupied oxygen neighboring polyhedra.

[100] and [001] directions by 11 and 5 atomic planes, respectively (see 1/8B model in Figure 2). Calculated Li–Li interatomic distances are 9.68, 4.89, and 6.49 Å along the [100], [010], and [001] directions, respectively. The corresponding intercalation process is accompanied by the largest enlargement in the *b* supercell parameter for $x = 1/8$ (see Figure 5). Structural distortions due to lithium insertion are very similar to distortions observed at $x = 1/16$. Indeed, the Li–O_{eq} interatomic distances are within 2.23 ± 0.03 Å while the Li–O_{ap} distances are calculated to be 1.86 Å. Neighboring oxygen octahedra are also found to exhibit similar distortions as octahedra at $x = 1/16$. The only exception is in the [010] direction which is occupied at $x = 1/8$. Although the same distortion pattern holds for the Sn–Sn distance, it differs at $x = 1/16$ in magnitude and calculation shows increases of 0.47, 0.15, and 0.04 Å along the [100], [010], and [001] directions, respectively. Moreover, for $x = 1/8$, the next most stable Li ordering is the placement of Li atoms in adjacent positions along the *c*-direction (1/8A). Therefore, structures with lithium atoms arranged along *c* channels have energies slightly higher than those of the same *ab*-layered structures. However,

structures with lithium atoms arranged in the second neighbor site along consecutive *ab*-planes (1/8C) are somewhat less stable. The less stable configurations correspond to two lithium ions in the 2 × 2 × 2 supercell which are located in opposite sites of (i) two consecutive *bc*-planes while in the same *ab*-plane (1/8E, E_{coh} = 287.7 eV) and (ii) two consecutive *bc*- and *ab*-planes (1/8F, E_{coh} = 286.6). Interestingly, the largest Li–Li distance between the two lithium atoms in the 2 × 2 × 2 supercell is visible in models 1/8E and 1/8F.

For $x = 1/4$, the stability order is as follows: 1/4C < 1/4B < 1/4H < 1/4A < 1/4D < 1/4E ≈ 1/4G < 1/4F. The lowest-energy ordering (1/4F) occurs when lithium ions are inserted in the consecutive *ab*-planes but arranged diagonally to each other within the *bc*-plane and are separated by 5, 5, and 3 atomic planes in the [100], [010], and [001] directions, respectively. Distortions around the intercalation site are also similar to distortions found for more diluted models. The oxygen octahedron around the lithium atom shrinks by 2.6% (see Table 2). Indeed, the calculated Li–O_{eq} interatomic distances are within 2.20 ± 0.04 Å while the Li–O_{ap} distances are 1.90 Å. Sn–Sn interatomic distances are enlarged by 0.60 and 0.25 Å along the [100] and [010] directions, respectively. A rather tiny variation is predicted along the [001] direction. At the 1/4F ordering scheme, oxygen octahedra of Li-occupied sites share edges in the [001] direction. This packing results in a more significant expansion of neighboring unoccupied oxygen octahedral, i.e., a volume variation of 14.6% in the [110]-glide neighboring octahedron and 11.9% in the oxygen polyhedra along the [010] and [001] directions.

The lowest-energy configuration at $x = 1/2$ is provided by model 1/2B. In this Li ordering, lithium atoms are separated from each other by 3, 1, and 1 atomic layers along the [100], [010], and [001] directions. The corresponding Li–Li distances are calculated to be 6.04, 6.01, and 6.55 Å, respectively. The Li–O_{eq} (2.24 ± 0.04 Å) and Li–O_{ap} (1.94 Å) distances are slightly larger than the distances found for more diluted concentrations. This ordering of the Li ion causes a uniform and large expansion (15.0%) in the [010]-, [100]-, and [001]-glide (vacant) neighboring oxygen octahedra. Very large lattice distortions are reflected in Sn–Sn atomic distances. Again, the largest expansion (1.06 Å) is observed in the Sn–Sn distance along the [100] direction, whereas the distances along [010] and [001] directions are 0.34 and 0.09 Å, respectively. The less stable configuration for this composition, 1/2C, occurs when the lattice is fully lithiated in *ab*-planes with unoccupied neighboring sites along the [001] direction.

Despite our efforts to optimize a number of several different orderings of Li ions for $x = 1$, the only stable configuration we have found is where lithium atoms are separated by 3, 1, and 5 atomic layers along [100], [010], and [001] directions,

respectively. In this concentration, the arrangement of oxygen atoms around the lithium ion is significantly changed. Actually, two distinct oxygen octahedra are observed which differ from each other with respect to the Li−O_{eq} distances of 2.21 Å in an intercalation site and 2.32 Å in a [110] glide octahedron. The Li−O_{ap} distance is 2.26 Å and therefore is larger than the distance found for more diluted systems. Upon lithium intercalation, Sn−Sn distances increase 0.72 and 0.62 Å along the [100] and [010] directions, respectively, but decrease 0.17 Å along the [001] direction (see Figure 5).

3.3. Electronic Properties of Lithiated SnO_2. We have assessed the effects of lithium intercalation on the electronic properties of tin oxide by analyzing electronic band structure, DOS and PDOS diagrams, and Mulliken populations in Li_xSnO_2 systems.

Electronic band structures for different Li concentrations were found to exhibit the same topology and differ only in their magnitudes. To give an example, a band structure diagram for x = 0.5 is shown in Figure 7. For comparison purposes, Figure 7
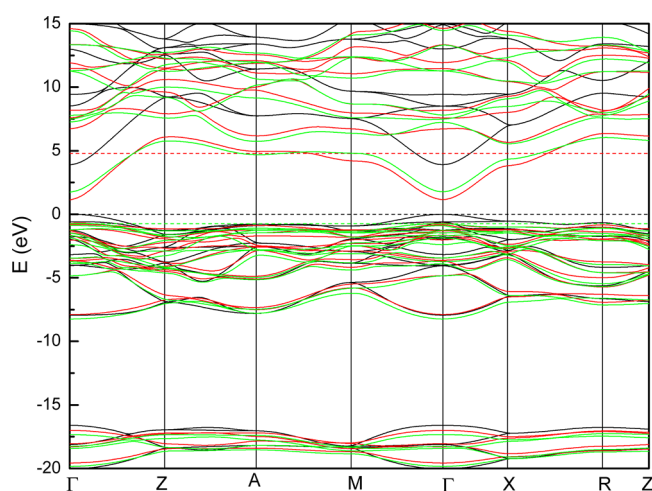

Figure 7. Calculated 1-cell electronic band structure diagrams for (i) pure SnO_2 (black line), $Li_{0.5}SnO_2$ (red line), and Li_0SnO_2 (green line, see text for details about this model). The dashed lines refer to the corresponding Fermi level.

depicts the band structure of pure SnO_2 (black line) and $Li_{0.5}SnO_2$ (red line). The green line corresponds to the electronic band structure of Li_0SnO_2 where Li_0SnO_2 is a delithiated SnO_2 crystal expanded to the same dimensions as $Li_{0.5}SnO_2$ (see discussion below). In the following discussion, the energy zero for all materials is the Fermi level of pure SnO_2, i.e., its highest energy eigenstate. Fermi energies are indicated by the corresponding black, red, or green dashed lines. For each diagram three groups of bands can be distinguished. The first band consists of 12 valence bands immediately below the Fermi level of pure SnO_2 (VB1); the second group is formed by four bands (VB2) below VB1, and conduction bands are grouped in the third group (CB). It is verified that no new band is induced in VB1, VB2, or CB by lithium intercalation.

It is well-known that changes in band structure induced by ion intercalation can be due to structural (e.g., lattice expansion) and electronic (e.g., chemical reduction) effects. To differentiate these two effects, we include in Figure 7 the band structure diagram of Li_0SnO_2 (as mentioned above). For clarity, we provide as Supporting Information the superimposed band structures of SnO_2 and $Li_{0.5}SnO_2$ (Figure S3), SnO_2 and

Li_0SnO_2 (Figure S4), and Li_0SnO_2 and $Li_{0.5}SnO_2$ (Figure S5). Thus, we can discern the structural effects induced by Li intercalation by comparing the green and black lines, whereas the electronic effects can be differentiated from the structural ones by comparing green and red lines.

The energy difference between the valence-band maximum and conduction-band minimum (at the Γ point) which is calculated to be 3.9 eV in pure SnO_2 decreases to 1.8 eV in lithiated $Li_{0.5}SnO_2$. This shift is predominantly caused by lattice expansion. Indeed, a 2.7 eV downward shift of the lowest conduction band in CB as well as a 0.70 downward shift of the highest band valence in VB1 are mainly due to structural changes. The VB1 width is found to decrease upon lithium intercalation from 7.96 eV in pure SnO_2 to 7.19 eV in $Li_{0.5}SnO_2$. However, this feature is due to structural as well as electronic effects. The electronic effect induced by lithium intercalation can be clearly distinguished by comparing the band structures of Li_0SnO_2 (green line) and $Li_{0.5}SnO_2$ (red line). Li intercalation has proven to yield metallic properties as long as the electrons donated to the lattice result in a rise of the Fermi level. An analysis of the PDOS (see discussion below) reveals that the lowest energy conduction band in CB is predominantly composed of Sn 5s and Sn 5p orbitals. Thus, our calculations predict that the charge transfer from lithium to a Sn 5s- and Sn 5p-based CB crystal orbital should induce metallic properties.

The distance in energy between the highest electronic level in VB2 and the lowest electronic level in VB1 (calculated to be 8.7 eV in pure SnO_2) increases to 9.1 eV in $Li_{0.5}SnO_2$.

The DOS and PDOS of SnO_2 and $Li_{0.5}SnO_2$ are compared in Figure 8. In this diagram only the upper valence band (VB1) and the conduction band (CB) are depicted. It can be observed that for both materials the valence bands are predominantly O 2p with a small admixture of Sn 5s (in the lower edge of VB1) and of 5p (in the upper edge of VB1). There is an even smaller contribution of Li 2s states to upper part of VB1 in $Li_{0.5}SnO_2$ (not shown in Figure 8). On the other hand, lower states in CB are connected to Sn 5s orbitals in SnO_2 and Sn 5s and Sn 5p orbitals in $Li_{0.5}SnO_2$. The main topological differences concerning the valence band due to lithium intercalation include (i) the dramatic reduction of the peak around −6 eV, which is predominantly composed of Sn 5s and Sn $5p_z$ orbitals, and (ii) an increase in the magnitude of the peak centered at −3.7 eV, which is due to the increased contribution of the Sn $5p_y$ orbital to the peak.

We have rationalized these features in terms of structural and electronic effects induced by lithium intercalation. The total and atom-projected DOS of SnO_2, $Li_{0.5}SnO_2$, and delithiated Li_0SnO_2 are presented as Figures S6, S7, and S8, respectively, in the Supporting Information. A comparison of the DOS diagrams of SnO_2 and Li_0SnO_2 reveals that lattice expansion accounts for the first effect (reduction of Sn 5s and Sn $5p_z$ contributions to the peak). The conspicuous peak at −6 eV in the DOS of SnO_2 is not noticeable in the DOS of Li_0SnO_2. The remaining effect is electronic in nature, and it can be clearly identified by comparing the DOS diagram of the $Li_{0.5}SnO_2$ (Figure S7) and the Li_0SnO_2 (Figure S8).

As mentioned above, the VB1 bandwidth decreases about 0.8 eV upon lithium intercalation (from 7.96 to 7.19 eV). The narrowing of VB1 which is predominantly constituted by O 2p orbitals is expected to decrease the effective overlap between the O 2p and Sn 5s/Sn 5p orbitals.
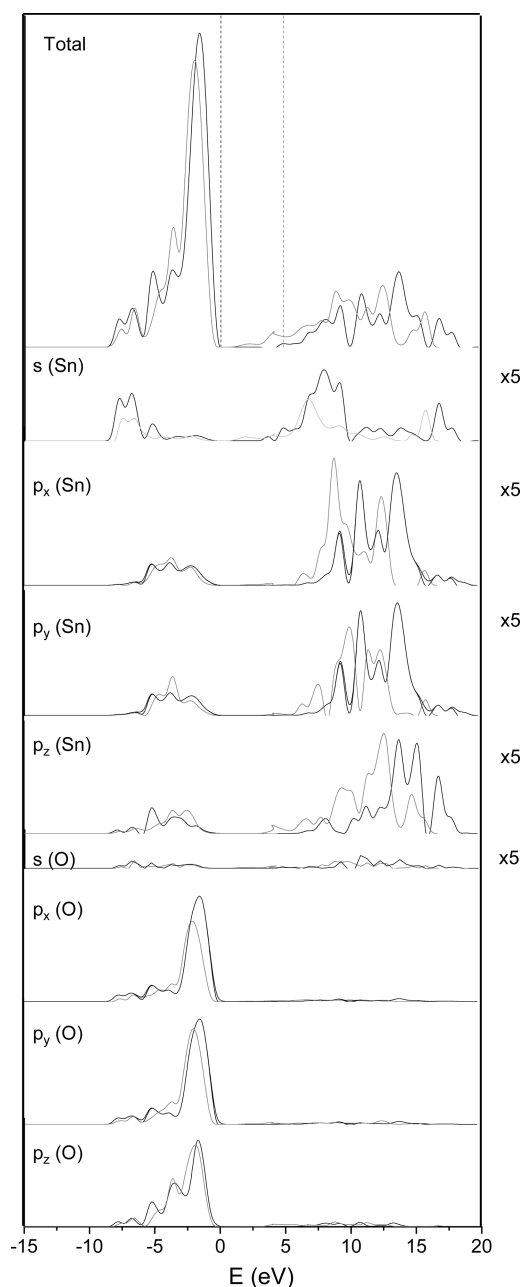
Figure 8. Calculated 1-cell DOS and PDOS of SnO_2 (heavy lines) and $Li_{0.5}SnO_2$ (light lines). The dashed lines indicate the corresponding Fermi energies.

Figure 9. Energy difference between the valence-band maximum and conduction-band minimum of lithiated SnO_2 as a function of the concentration of Li ion.

Table 3. Calculated Mulliken Charges on the Li Center for the Most Stable Li_xSnO_2 Systems and Relative Amounts of Charge (in percentage) Retained by the Li Ion as Well as Charges Transferred to the Sn and O Atoms

	$x = 1/16$	$x = 1/8$	$x = 1/4$	$x = 1/2$	$x = 1$
q_M(Li)	0.73	0.73	0.72	0.69	0.68
%(Li)	26.9	27.4	28.1	30.8	32.5
%(Sn)	73.1	70.1	55.5	44.3	36.0
%(O)	0	2.5	16.4	24.9	31.5

$x = 1/16$ to $x = 1$ (first line in Table 3). Nevertheless, the distribution pattern related to the charge transfer from the Li atom to the SnO_2 host is very dependent upon the Li content. The second to fourth rows in Table 3 are the relative amounts (in percentage) of the charge retained by Li ions and the charges transferred to Sn and O atoms. Clearly, as long as the Li content increases, the relative amount of charge transferred to the tin atom decreases, whereas the charge transferred to the oxygen atom increases. Moreover, the charge distribution throughout Sn and O atoms is not homogeneous. The majority of charges are located on Sn sites neighboring the Li ion. Regarding oxygen atoms, apical oxygen atoms receive a larger amount of electrons than the equatorial atoms.

The analysis of Mulliken charges is consistent with the chemical reduction of SnO_2 as a result of Li intercalation. It is worth noting that it has been proposed that the formal valence of tin in its oxidized forms (e.g., SnO and SnO_2) can be distinguished from each other by the separation in energy of the Sn 4d peak from the most prominent (leading) peak of the valence band.[74,75] Indeed, in an X-ray-photoemission spectroscopy study, Sherwood found that in SnO the most intense peak in the valence band is separated by 23.7 eV from the Sn 4d core peak, but this separation falls to 21.1 eV in SnO_2.[74] Still, Themlin and co-workers found an energy difference of 23.1 eV for SnO and 21.5 for SnO_2.[75] Therefore, we looked for evidence of the chemical reduction of tin oxide induced by lithium intercalation by comparing the DOS of SnO_2 (Figure S6) and $Li_{0.5}SnO_2$ (Figure S7). Contrary to expectations, the calculated difference energy between the Sn 4d level and the leading peak on the valence band was found to be the same (21.2 eV) in passing from SnO_2 to $Li_{0.5}SnO_2$. However, it should be taken into account that changes in the DOS diagram caused by ion intercalation might be due to structural as well as electronic effects. Thus, noticeable differences in XPS spectra of SnO_2 and SnO are expected to be determined by these two

Figure 9 shows the variation of the lithiated SnO_2 band gap with the concentration of the Li ion. The band-gap energy has been calculated as the difference between the valence band maximum and the conduction band minimum using our large 2 × 2 × 2 cell.

Mulliken population was used to assess the charge rearrangement induced by the Li intercalation, and the corresponding values are reported in Table 3. They are only a guide to the total electronic density at a given atomic center. However, differences in their magnitude are a reasonable measure of the change in the electron density, and it is precisely this change which interests us. In Li_xSnO_2, lithium is significantly ionized. However, its charge does not vary appreciably with the Li content. Mulliken charges on the lithium center range between 0.73 and 0.68 in proceeding from
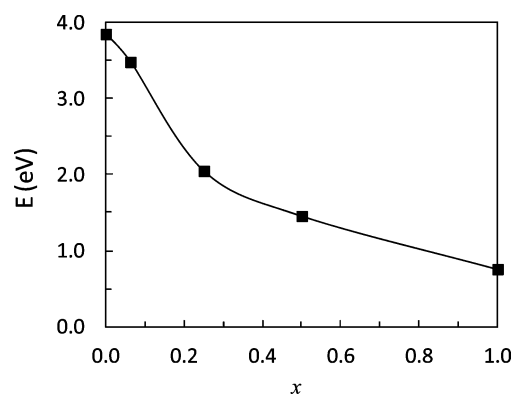
contributions since the two oxides are structurally different. However, we can discern the chemical reduction induced by Li intercalation by comparing the DOS diagram of $Li_{0.5}SnO_2$ (Figure S7) and delithiated Li_0SnO_2 (Figure S8) models, inasmuch as the structural influence is isolated. Thus, an increase is realized in the separation between the Sn 4d peak and the leading peak of the valence band in progressing from $Li_{0.5}SnO_2$ (21.2 eV) to delithiated Li_0SnO_2 (22.1 eV); i.e., chemical reduction is predicted to decrease rather than increase the separation between the near-core region (Sn 4d) and the valence-band region (O 2p). On the other hand, a comparison between DOS diagrams of SnO_2 (Figure S6) and delithiated Li_0SnO_2 (Figure S8) permits identification of the role of structural expansion in the electronic structure of the host. It is clear from such a comparison that lattice expansion increases the separation from 21.2 eV in SnO_2 to 22.1 eV in delithiated in Li_0SnO_2. Thus, two opposite and competitive effects govern the separation between Sn 4d and O 2p (most prominent) peaks in SnO_2 upon Li intercalation; the lattice expansion increases the separation while the chemical reduction decreases it. Our results reveal that even though the formal valencies (Sn^{2+} and Sn^{4+}) of tin in their oxides can be discerned via observance of the separation of the features in the valence band from the near-core region, the characterization of the chemical reduction in ion-intercalated SnO_2 via such an approach may not be affordable unless structural and electronic effects are discerned and individually quantified.

3.4. Li-Ion Diffusion. As mentioned above, the most reasonable diffusion processes involve the jump of a Li atom between two adjacent octahedral sites and may occur along the [110] direction (in the *ab*-plane) or along open [001] channels (the *c*-direction).

In the *ab*-plane, the Li atom moves between two octahedral sites located at (0.0, 0.25, *z*) and (0.25, 0.5, *z*) positions. The corresponding energetic profiles for the compositions considered (*x* = 1/16, 1/8, and 1/4) are illustrated in Figure 10.
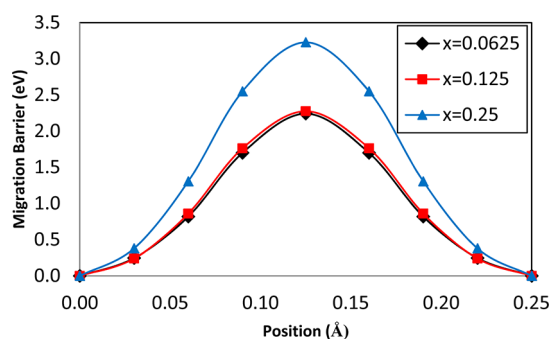
Figure 10. Calculated minimum-energy paths for Li-ion hopping between adjacent octahedral intercalation sites along the [110] direction at distinct Li content.

Figure 10 shows that calculated diffusion barrier energies are somewhat Li content dependent. The lithium diffusion process implies migration to an adjacent vacant octahedral site by a straight direct path with ~3.5 Å of hopping distance. The transition state is situated at the midpoint connecting the octahedral interstitial sites. In jumping from an octahedral site to an adjacent site, the Li ion passes by two equatorial oxygen atoms (see Figure 3). The distance between these two oxygen atoms is affected by the Li hopping. The distance decreases from 3.219 Å (in pure SnO_2) to 3.051, 3.083, and 3.015 Å at *x*

= 1/16, 1/8, and 1/4, respectively. In the transition state of diffusion, the Li atom is surrounded by four O and three Sn atoms. The corresponding distances are listed in Table 4 for all

Table 4. Calculated Li−O and Li−Sn Distances (in Å) When the Li Atom Is Situated in the Middle Position of the Path along the [110] Direction[a]

	x = 1/16	*x* = 1/8	*x* = 1/4
Li−O	1.692(2)	1.705(2)	1.782(2)
	1.992(1)	2.006(1)	2.224(1)
	2.679(1)	2.698(1)	2.838(1)
Li−Sn	2.235(1)	2.236(1)	1.942(1)
	2.377(2)	2.374(2)	2.503(2)

[a]The multiplicity of the bonds is indicated in parentheses.

the composition studied. The diffusion path is shown schematically in Figure 3a. In particular, in transition state structures, the Li atom is quite close to the two oxygens at distances of 1.692, 1.705, and 1.782 Å at *x* = 1/16, 1/8, and 1/ 4, respectively.

The barrier energy increases from 2.24 eV at *x* = 1/16 to 2.28 eV at *x* = 1/8 and to 3.23 eV at *x* = 1/4. Therefore, the Li diffusion process will be less favorable with increasing concentration. It is worth noting that for *x* = 1/2 there is no possibility of performing any Li diffusion along the [110] direction, since these positions are occupied by other Li atoms in more stable configurations. Assuming a typical value for the jump frequency of 10^{13} s^{-1}, a temperature of 600 °C, a hopping distance of ~3.5 Å, and using the above values for the barriers, diffusion coefficients are computed to be 1.40×10^{-15} cm^2/s at *x* = 0.0625, 8.88×10^{-15} cm^2/s at *x* = 0.125, and 2.83×10^{-21} cm^2/s at *x* = 0.25, respectively.

In the *c*-direction, the Li atom moves along the segment that connects two octahedral sites at (*x*, *y*, 0.0) and (*x*, *y*, 0.25) positions. The corresponding energetic profiles for the selected Li content are presented in Figure 11, and the diffusion path is depicted schematically in Figure 3b.

The corresponding calculated energy barriers are as follows: 0.37, 0.38, 0.49, and 0.52 eV at *x* = 1/16, 1/8, 1/4, and 1/2, respectively. First, all these energy values are significantly lower than the values predicted for diffusion along *ab*-plane ([110] direction) because diffusion along the *c* ([001]) direction is
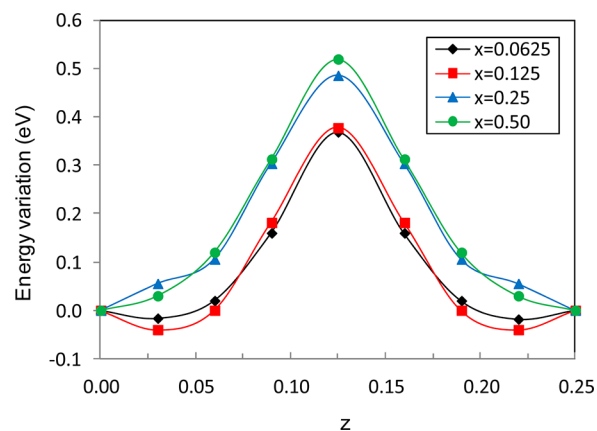
Figure 11. Calculated energetic profile related to the Li diffusion between adjacent octahedral intercalation sites along the [001] direction at selected Li content.

related to more open channels. Second, the barrier energy also increases with increasing Li content. For a hopping distance of 1.625 Å, diffusion coefficients are computed to be 1.96×10^{-5}, 1.74×10^{-5}, 4.13×10^{-6}, and 2.63×10^{-6} cm^2/s at $x = 1/16$, 1/8, 1/4, and 1/2, respectively. Therefore, our results show that in rutile SnO$_2$ the Li diffusion is strongly anisotropic since it is dominated by diffusion in the [001] direction. This finding is in line with experimental[76] and theoretical[77,78] studies concerning Li diffusion into the rutile TiO$_2$ which indicate that $D_{[110]} \ll D_{[001]}$ by a factor of at least 10^8 up to 550 °C.[76]

4. CONCLUSION

We have modeled the electronic and structural properties of lithiated SnO$_2$ systems for several concentrations and ordering of Li ions by performing periodic DFT calculations with large supercells. We have demonstrated that (i) structural relaxation in SnO$_2$ induced by Li intercalation is highly anisotropic, (ii) lithium is significantly ionized in lithiated SnO$_2$, (iii) Li intercalation causes chemical reduction in SnO$_2$ and yields metallic properties, (iv) the energy difference between the top of the valence band and the bottom of the conduction band of Li$_x$SnO$_2$ systems decreases with Li-ion concentration, (v) Li diffusion along the c-direction is favored with respect to diffusion taking place along ab-planes, and (vi) increasing the Li-ion concentration results in an increase the activation energy for diffusion along ab-planes as well as along the c-direction.

■ ASSOCIATED CONTENT

ⓢ Supporting Information

(i) Fractional coordinates of intercalation sites through each periodic model, (ii) superimposed electronic band structures (SnO$_2$ and Li$_{0.5}$SnO$_2$, SnO$_2$ and Li$_0$SnO$_2$, and Li$_0$SnO$_2$ and Li$_{0.5}$SnO$_2$), and (iii) total and atom-projected DOS of SnO$_2$, Li$_{0.5}$SnO$_2$, and delithiated Li$_0$SnO$_2$. This material is available free of charge via the Internet at http://pubs.acs.org.

■ AUTHOR INFORMATION

Corresponding Author
*E-mail: fabricio.sensato@unifesp.br (F.R.S.); lgracia@qfa.uji.es (L.G.).
Notes
The authors declare no competing financial interest.

■ ACKNOWLEDGMENTS

■ REFERENCES

(1) Kamat, P. V. *J. Phys. Chem. Lett.* **2010**, *1*, 2220−2221.
(2) Whittingham, M. *Chem. Rev.* **2004**, *104*, 4271−4301.
(3) Idota, Y.; Mishima, M.; Miyaki, M.; Kubota, T.; Misayaka, T. Eur. Pat. Appl. 651450, A1, 950503.
(4) Idota, Y.; Kubota, T.; Matsufuji, A.; Maekawa, Y.; Miyasaka, T. *Science* **1997**, *276*, 1395−1397.
(5) Lou, X.; Deng, D.; Lee, J.; Archer, L. *Chem. Mater.* **2008**, *20*, 6562−6566.
(6) Bueno, P.; Leite, E. *J. Phys. Chem. B* **2003**, *107*, 8868−8877.
(7) Bueno, P.; Leite, E.; Giraldi, T.; Bulhoes, L.; Longo, E. *J. Phys. Chem. B* **2003**, *107*, 8878−8883.
(8) Chaparadza, A.; Rananavare, S.; Shutthanandan, V. *Mater. Chem. Phys.* **2007**, *102*, 176−180.
(9) Kim, C.; Noh, M.; Choi, M.; Cho, J.; Park, B. *Chem. Mater.* **2005**, *17*, 3297−3301.
(10) Li, N. C.; Martin, C. R.; Scrosati, B. *J. Power Sources* **2001**, *97−8*, 240−243.
(11) Lytle, J. C.; Yan, H. W.; Ergang, N. S.; Smyrl, W. H.; Stein, A. *J. Mater. Chem.* **2004**, *14*, 1616−1622.
(12) Park, M. S.; Wang, G. X.; Kang, Y. M.; Wexler, D.; Dou, S. X.; Liu, H. K. *Angew. Chem., Int. Ed.* **2007**, *46*, 750−753.
(13) Wang, Y.; Lee, J. Y. *J. Phys. Chem. B* **2004**, *108*, 17832−17837.
(14) Ying, Z.; Wan, Q.; Cao, H.; Song, Z. T.; Feng, S. L. *Appl. Phys. Lett.* **2005**, *87*, 113108.
(15) Sivashanmugam, A.; Premkumar, T.; Gopukumar, S.; Renganathan, N. G.; Wohlfahrt-Mehrens, M.; Garche, J. *J. Appl. Electrochem.* **2005**, *35*, 1045−1050.
(16) Sun, X. M.; Liu, J. F.; Li, Y. D. *Chem. Mater.* **2006**, *18*, 3486−3494.
(17) Deng, D.; Lee, J. Y. *Chem. Mater.* **2008**, *20*, 1841−1846.
(18) Olivi, P.; Pereira, E. C.; Longo, E.; Varella, J. A.; Bulhões, L. O. D. *J. Electrochem. Soc.* **1993**, *140*, L81−L82.
(19) Huang, J. Y.; Zhong, L.; Wang, C. M.; Sullivan, J. P.; Xu, W.; Zhang, L. Q.; Mao, S. X.; Hudak, N. S.; Liu, X. H.; Subramanian, A.; Fan, H.; Qi, L.; Kushima, A.; Li, J. *Science* **2010**, *330*, 1515−1520.
(20) Zhang, L. Q.; Liu, X. H.; Liu, Y.; Huang, S.; Zhu, T.; Gui, L.; Mao, S. X.; Ye, Z. Z.; Wang, C. M.; Sullivan, J. P.; Huang, J. Y. *ACS Nano* **2011**, *5*, 4800−4809.
(21) Zhu, J. J.; Lu, Z. H.; Aruna, S. T.; Aurbach, D.; Gedanken, A. *Chem. Mater.* **2000**, *12*, 2557−2566.
(22) Xia, G. F.; Li, N.; Li, D. Y.; Liu, R. Q.; Xiao, N.; Tian, D. *Mater. Lett.* **2011**, *65*, 3377−3379.
(23) Yim, C. H.; Baranova, E. A.; Courtel, F. M.; Abu-Lebdeh, Y.; Davidson, I. J. *J. Power Sources* **2011**, *196*, 9731−9736.
(24) Subramanian, V.; Burke, W. W.; Zhu, H. W.; Wei, B. Q. *J. Phys. Chem. C* **2008**, *112*, 4550−4556.
(25) Orel, B.; Lavrencicstangar, U.; Kalcher, K. *J. Electrochem. Soc.* **1994**, *141*, L127−L130.
(26) Isidorsson, J.; Granqvist, C. G.; Haggstrom, L.; Nordstrom, E. *J. Appl. Phys.* **1996**, *80*, 2367−2371.
(27) Felde, U.; Haase, M.; Weller, H. *J. Phys. Chem. B* **2000**, *104*, 9388−9395.
(28) Isidorsson, J.; Lindstrom, T.; Granqvist, C. G.; Herranen, M. *J. Electrochem. Soc.* **2000**, *147*, 2784−2795.
(29) Isidorsson, J.; Granqvist, C. G.; von Rottkay, K.; Rubin, M. *Appl. Opt.* **1998**, *37*, 7334−7341.
(30) Orel, B.; Krasovec, U. O.; Stangar, U. L.; Judeinstein, P. *J. Sol-Gel Sci. Technol.* **1998**, *11*, 87−104.
(31) Isidorsson, J.; Granqvist, C. G. *Sol. Energy Mater. Sol. Cells* **1996**, *44*, 375−381.
(32) Winter, M.; Besenhard, J. O.; Spahr, M. E.; Novak, P. *Adv. Mater.* **1998**, *10*, 725−763.
(33) Courtney, I. A.; Dahn, J. R. *J. Electrochem. Soc.* **1997**, *144*, 2045−2052.
(34) Dunlap, R. A.; Small, D. A.; MacNeil, D. D.; Obrovac, M. N.; Dahn, J. R. *J. Alloys Compd.* **1999**, *289*, 135−142.
(35) Chao, S. C.; Yen, Y. C.; Song, Y. F.; Chen, Y. M.; Wu, H. C.; Wu, N. L. *Electrochem. Commun.* **2010**, *12*, 234−237.
(36) Winter, M.; Besenhard, J. O. *Electrochim. Acta* **1999**, *45*, 31−50.
(37) Sensato, F. R. *J. Comput-Aided Mater. Des.* **2005**, *12*, 91−92.
(38) Sandu, I.; Brousse, T.; Schleich, D. M.; Danot, M. *J. Solid State Chem.* **2004**, *177*, 4332−4340.
(39) Beltran, A.; Andres, J.; Longo, E.; Leite, E. R. *Appl. Phys. Lett.* **2003**, *83*, 635−637.
(40) Gracia, L.; Beltran, A.; Andres, J. *J. Phys. Chem. B* **2007**, *111*, 6479−6485.
(41) Sensato, F. R.; Custodio, R.; Calatayud, M.; Beltran, A.; Andres, J.; Sambrano, J. R.; Longo, E. *Surf. Sci.* **2002**, *511*, 408−420.

(42) Sensato, F.; Filho, O.; Longo, E.; Sambrano, J.; Andres, J. *J. Mol. Struct.: THEOCHEM* **2001**, *541*, 69−79.

(43) Sensato, F.; Custodio, R.; Longo, E.; Beltran, A.; Andres, J. *Catal. Today* **2003**, *85*, 145−152.

(44) Stroppa, D. G.; Montoro, L. A.; Beltran, A.; Conti, T. G.; da Silva, R. O.; Andres, J.; Longo, E.; Leite, E. R.; Ramirez, A. J. *J. Am. Chem. Soc.* **2009**, *131*, 14544−14548.

(45) Perdew, J. P.; Wang, Y. *Phys. Rev. B* **1992**, *45*, 13244−13249.

(46) Kresse, G.; Hafner, J. *Phys. Rev. B* **1994**, *49*, 14251−14269.

(47) Kresse, G.; Furthmuller, J. *Comput. Mater. Sci.* **1996**, *6*, 15−50.

(48) Kresse, G.; Joubert, D. *Phys. Rev. B* **1999**, *59*, 1758−1775.

(49) Lee, C. T.; Yang, W. T.; Parr, R. G. *Phys. Rev. B* **1988**, *37*, 785−789.

(50) Becke, A. D. *J. Chem. Phys.* **1993**, *98*, 5648−5652.

(51) Dovesi, R.; Saunders, V. R.; Roetti, C.; Orlando, R.; Zicovich-Wilson, C. M.; Pascale, F.; Civalleri, B.; Doll, K.; Harrison, N. M.; Bush, I. J.; D'Arco, P.; Llunell, M. *CRYSTAL09 User's Manual*; University of Torino: Torino, 2009.

(52) Dovesi, R.; Orlando, R.; Civalleri, B.; Roetti, C.; Saunders, V. R.; Zicovich-Wilson, C. M. *Z. Kristallogr.* **2005**, *220*, 571−573.

(53) Muscat, J.; Wander, A.; Harrison, N. M. *Chem. Phys. Lett.* **2001**, *342*, 397−401.

(54) Towler, M. D. TCM Crystal basis set library: http://www.tcm.phy.cam.ac.uk/~mdt26/crystal.html (accessed June 18, 2012.)

(55) Corno, M.; Busco, C.; Civalleri, B.; Ugliengo, P. *Phys. Chem. Chem. Phys.* **2006**, *8*, 2464−2472.

(56) Merawa, M.; Labeguerie, P.; Ugliengo, P.; Doll, K.; Dovesi, R. *Chem. Phys. Lett.* **2004**, *387*, 453−459.

(57) Kang, K.; Ceder, G. *Phys. Rev. B* **2006**, *74*, 094105.

(58) Miao, S.; Kocher, M.; Rez, P.; Fultz, B.; Yazami, R.; Ahn, C. C. *J. Phys. Chem. A* **2007**, *111*, 4242−4247.

(59) Ouyang, C. Y.; Shi, S. Q.; Wang, Z. X.; Huang, X. J.; Chen, L. Q. *Phys. Rev. B* **2004**, *69*, 104303.

(60) Ouyang, C. Y.; Shi, S. Q.; Wang, Z. X.; Li, H.; Huang, X. J.; Chen, L. Q. *Europhys. Lett.* **2004**, *67*, 28−34.

(61) Kishida, I.; Koyama, Y.; Kuwabara, A.; Yamamoto, T.; Oba, F.; Tanaka, I. *J. Phys. Chem. B* **2006**, *110*, 8258−8262.

(62) Iddir, H.; Ogut, S.; Zapol, P.; Browning, N. D. *Phys. Rev. B* **2007**, *75*, 073203.

(63) Tielens, F.; Calatayud, M.; Beltran, A.; Minot, C.; Andres, J. *J. Electroanal. Chem.* **2005**, *581*, 216−223.

(64) Anicete-Santos, M.; Gracia, L.; Beltran, A.; Andres, J.; Varela, J. A.; Longo, E. *Phys. Rev. B* **2008**, *77*, 085112.

(65) Gracia, L.; Garcia-Canadas, J.; Garcia-Belmonte, G.; Beltran, A.; Andres, J.; Bisquert, J. *Electrochem. Solid-State Lett.* **2005**, *8*, J21−J23.

(66) Gracia, L.; Calatayud, M.; Andres, J.; Minot, C.; Salmeron, M. *Phys. Rev. B* **2005**, *71*, 033407.

(67) Peng, G. W.; Huan, A. C. H.; Tok, E. S.; Feng, Y. P. *Phys. Rev. B* **2006**, *74*, 195335.

(68) Baur, W. H. *Acta Crystallogr.* **1956**, *9*, 515−520.

(69) Haines, J.; Leger, J. M. *Phys. Rev. B* **1997**, *55*, 11144−11154.

(70) Lee, C.; Ghosez, P.; Gonze, X. *Phys. Rev. B* **1994**, *50*, 13379−13387.

(71) Peercy, P. S.; Morosin, B. *Phys. Rev. B* **1973**, *7*, 2779−2786.

(72) Katiyar, R. S.; Dawson, P.; Hargreav, M.; Wilkinso, G. R. *J. Phys. C: Solid State Phys.* **1971**, *4*, 2421−1431.

(73) Cheng, B.; Xie, C.; Fang, L.; Xiao, Y.; Lei, S. *Mater. Chem. Phys.* **2011**, *129*, 713−717.

(74) Sherwood, P. M. A. *Phys. Rev. B* **1990**, *41*, 10151−10154.

(75) Themlin, J. M.; Chtaib, M.; Henrard, L.; Lambin, P.; Darville, J.; Gilles, J. M. *Phys. Rev. B* **1992**, *46*, 2460−2466.

(76) Johnson, O. W. *Phys. Rev.* **1964**, *136*, A284−A290.

(77) Koudriachova, M. V.; Harrison, N. M.; de Leeuw, S. W. *Phys. Rev. Lett.* **2001**, *86*, 1275−1278.

(78) Koudriachova, M. V.; Harrison, N. M.; de Leeuw, S. W. *Phys. Rev. B* **2002**, *65*, 235423.